OEA | Opto-Electronic Advances

CN 51-1781/TN ISSN (Print) 2096-4579 ISSN (Online) 2097-3993

Heterogeneously integrated micro-ring with SnS_2 for dual-functional optical modulation and photodetection

Jinyi Du, Lidan Lu, Xu Zhang*, Bofei Zhu, Wenbo Bo, Yingjie Xu, Guang Chen, Yanlin He, Guanghui Ren*, Xiaoping Lou, Zheng You* and Lianqing Zhu*

Citation: Du JY, Lu LD, Zhang X, Zhu BF, Bo WB, Xu YJ, Chen G, He YL, Ren GH, Lou XP, You Z, Zhu LQ. Heterogeneously integrated micro-ring with SnS_2 for dual-functional optical modulation and photodetection. *Opto-Electron Adv* **9**, 260042 (2026).

https://doi.org/10.29026/oea.2026.260042

Received: 14 February 2026; Accepted: 21 April 2026; Published online: 9 May 2026

Related articles

Multi-dimensional photodetection: from material intrinsic properties and metasurface engineering to silicon photonic integration

Wenqi Liu, Zilan Tang, Qingzhao Hua et al

Opto-Electronic Technology 2026, **2**(1): 260001 doi: 10.29026/oet.2026.260001

Control of light–matter interactions in two-dimensional materials with nanoparticle-on-mirror structures

Shasha Li, Yini Fang, Jianfang Wang

Opto-Electronic Science 2024, **3**(7): 240011 doi: 10.29026/oes.2024.240011

Highly enhanced UV absorption and light emission of monolayer WS_2 through hybridization with Ti_2N MXene quantum dots and g-C_3N_4 quantum dots

Anir S. Sharbirin, Rebekah E. Kong, Wendy B. Mato et al

Opto-Electronic Advances 2024, **7**(6): 240029 doi: 10.29026/oea.2024.240029

Thin-film lithium niobate-based detector: recent advances and perspectives

Xiaoli Sun, Yuechen Jia, Feng Chen

Opto-Electronic Science 2025, **4**(12): 250028 doi: 10.29026/oes.2025.250028

More related articles in Opto-Electronic Journals Group website

Opto-Electronic Journals Group

https://www.oejournal.org

OE_Journal @OptoElectronAdv

This is an early view version and will be formally published in a coming issue with other articles in due time.

OEA | Opto-Electronic Advances

Article

2026, Vol. , No.

Open Access

Heterogeneously integrated micro-ring with SnS_2 for dual-functional optical modulation and photodetection

Jinyi Du[1†], Lidan Lu[1†], Xu Zhang[1*], Bofei Zhu[2], Wenbo Bo[1], Yingjie Xu[4], Guang Chen[1], Yanlin He[1], Guanghui Ren[3*], Xiaoping Lou[1], Zheng You[2*] and Lianqing Zhu[1*]

Abstract: Achieving simultaneous optical modulation and photodetection in a single device represents a key objective for advancing integrated photonics. However, fabricating such dual-functional devices remains challenging due to process complexity, material instability, and weak light–matter interaction. This work demonstrates a dual-functional device through the heterogeneous integration of few-layer SnS_2 onto a silicon-on-insulator (SOI) microring resonator. Using an electrode-engineered design that eliminates the need for external gate control or heterojunctions, the device achieves simultaneous light modulation and detection. This design not only simplifies fabrication but also maintains independent control ports, enabling real-time monitoring of the optical modulation state and paving the way for integrated feedback in on-chip photonic computing systems. The modulator achieves a modulation depth of 23 dB, while the photodetector shows a responsivity of 0.38 A/W at −2 V through a hot-carrier-assisted mechanism. This work provides a compact and versatile platform for multifunctional photonic integration, supporting the development of more efficient and reliable on-chip photonic computing.

Keywords: two-dimensional materials; photodetectors; silicon microring resonator; silicon photonics

DOI: 10.29026/oea.2026.260042 | CSTR: 32247.14.oea.2026.260042

Citation: Du JY, Lu LD, Zhang X et al. Heterogeneously integrated micro-ring with SnS_2 for dual-functional optical modulation and photodetection. *Opto-Electron Adv*, 260042 (2026).

1 Introduction

In optical neural network systems, photodetectors and optical modulators serve as two fundamental building blocks[1−3]. Photodetectors are responsible for converting optical signals into electrical currents, enabling monitoring of optical power and subsequent electronic processing. Optical modulators, conversely, imprint electrical signals onto optical carriers, allowing dynamic control of light transmission. Together, they are essential building blocks in most optoelectronic computing and communication systems. However, in conventional architectures, these two functions are implemented by discrete, physically separated devices —optical power is tapped through bypass waveguides, fed into a dedicated photodetector, and the resulting photocurrent is amplified and converted into a driving voltage before being applied to a separate modulator. This discrete-component link inevitably introduces substantial power consumption, increased latency, and fabrication complexity, posing fundamental bottlenecks for high-density optical computing systems[4−6].

To enable dual-functional optoelectronic units, the integration of photodetection and optical modulation within a single device offers a promising approach to address these technical challenges. This integration allows for more compact optical circuit layouts, simplified photonic network architectures, and improved flexibility in high-density optical routing. Consequently, the development of dual-functional devices represents both an incremental advancement in device integration and a critical step toward highly integrated optical computing platforms. The atomic-scale

Received: 14 February 2026
Accepted: 21 April 2026
Published online: 9 May 2026

[1]School of Instrumentation Science and Opto-Electronics Engineering, Beijing Information Science and Technology University, Beijing 100192, China; [2]The Department of precision instrument, Tsinghua University, Beijing 100084, China; [3]Integrated Photonics and Applications Centre (InPAC), RMIT University, Melbourne, Victoria 3000, Australia; [4]School of Instrument Science and Opto-Electronics Engineering, Hefei University of Technology, Hefei 230009, China.
[†]These authors contributed equally to this work.
*Correspondence: X Zhang, E-mail: ps20252806@bistu.edu.cn; GH Ren, E-mail: guanghui.ren@rmit.edu.au;
Z You, E-mail: yz-dpi@mail.tsinghua.edu.cn; LQ Zhu, E-mail: zhulianqing@bistu.edu.cn

This is an early view version and will be formally published in a coming issue with other articles in due time.

thickness and exceptional optoelectronic properties of 2D materials—including gate-tunable Fermi levels, strong light-matter interaction, and broadband response —make them particularly suitable for co-integrating detection and modulation functionalities within a single waveguide platform[7]. A variety of two-dimensional materials, including black phosphorus[8–10], MoS_2[11–12], and $PtSe_2$[13], have been heterogeneously integrated with waveguides to achieve photodetection and optical modulation in the near-infrared band[14–16]. Across all these material systems, however, a common trade-off persists: achieving high-performance detection and modulation within a single device inevitably necessitates compromises among speed, modulation depth, responsivity, or fabrication complexity. To this end, researchers have extensively explored dual-functional devices based on heterogeneous integration of two-dimensional materials with silicon photonic waveguides[17–19]. Graphene, as the most extensively studied two-dimensional material[20–23], enabled the first demonstration of a monolayer-graphene-based dual-functional device on a silicon waveguide platform. Nevertheless, its responsivity remains only 57 mA/W, and the scheme imposes stringent requirements on the integrity of monolayer graphene[5]. Moreover, its zero-bandgap nature leads to difficulty in suppressing dark current, and the modulation relies on continuous gate voltage. Subsequently, a graphene/silicon heterojunction integrated on a p-n-doped silicon microring was demonstrated to achieve responsivity (>200 mA/W) and low modulation power, yet it still requires p-n junction doping and gate voltage control[3]. The graphene/$MoTe_2$ heterojunction dual-functional device, for the first time, introduces band engineering into dual-functional device design. Leveraging the wide bandgap of $MoTe_2$, it achieves low insertion loss in the C-band and enables dynamic reconfiguration between modulation and detection functionalities through a single heterojunction with single bias polarity switching, simplifying the fabrication process. However, this approach still faces challenges in the fabrication process of two-dimensional heterostructures; its responsivity of 0.64 mA/W remains an order of magnitude lower than that of dedicated germanium photodetectors, and the switching between modulation and detection functions relies on bias polarity reversal[4]. Alternatively, the WS_2/HfS_2 heterojunction has been integrated on a silicon waveguide to enable mid-infrared dual-functionality via interlayer exciton absorption, yet its responsivity remains at the μA/W level and operation relies on all-optical pumping[24]. The ITO/Ge hybrid photonic-plasmonic dual-functional device achieves an innovative breakthrough at the architectural level. Yet, this scheme currently remains at the simulation validation stage, and critical issues such as interface state control and CMOS process compatibility in practical fabrication have not been experimentally verified[6]. In parallel, a PN-junction silicon microring integrated with phase-change material has been demonstrated to achieve both modulation and detection at 100 Gbps, but it requires high-temperature ion implantation and exhibits low responsivity (~0.007 A/W)[25]. Table 1 summarizes the performance metrics and key features of representative dual-functional devices.

In this work, to avoid reliance on gate-voltage control, strict monolayer requirements, and capacitive structures, we heterogeneously integrate SnS_2 onto a microring resonator, achieving both optical modulation and photodetection in a single device. In this compact device architecture, SnS_2 serves as the primary photoactive material, enabling photon-to-electron conversion for photodetection while reducing optical loss caused by the gold heating electrodes. Furthermore, the engineered Au electrode design facilitates efficient hot-carrier generation[11]. On one hand, the microring resonator's strong optical confinement enhances light-matter interactions with the 2D material, enabling infrared photodetection through hot carriers. On the other hand, localized refractive index modulation through the heating electrode enables optical modulation functionality. The

Table 1 | Comparison of dual-functional integrated photonic devices.

Structure	Modulation performance	Detection performance	Speed / Bandwidth	Function switching methods	Ref.
Dual-layer graphene FET on Si waveguide (MZI)	Modulation depth: 64% transmission at gate voltage 40 V	57 mA/W @ 1.55 μm	Modulator: 1 GHz; Detector: 1 GHz	Gate voltage tuning	ref.[5]
WS_2/HfS_2 heterojunction on waveguide	All-optical modulation (visible pump control)	~50 μA/W @ 3.8–5.5 μm	Detector fall time: 1.07 μs / 22.1 μs ; modulator: 400 Hz	All-optical	ref.[24]
Graphene/Si heterojunction on p-n-doped Si MRR	Modulation depth: 12 dB	200 mA/W @ 1.5 V bias, 1550 nm	N/A	Forward bias for modulation; Reverse bias for detection	ref.[3]
Graphene/$MoTe_2$ heterojunction on Si MRR	Modulation depth:26.7 dB	0.47–0.64 mA/W @ C-band	Modulator: 7.0 GHz	Positive bias for modulation; Negative bias for detection	ref.[4]
PN-junction Si MRR with Sb_2Se_3	4×100 Gbps	0.007 A/W	Modulator: 100 Gbps; Detector: 100 Gbps	Bias switching (modulator/detector); Sb_2Se_3 trimming	ref.[25]
SnS_2-on-Si MRR with three-electrode	Modulation depth: 23 dB @ 0.8 V	Responsivity: 0.38 A/W @ 1550 nm	Modulator: 3.4 μs / 6.9 μs; Detector.: 8.4 ms / 11.8 ms	Three-electrode bias switching; simultaneous dual-function in single MRR	This work

This is an early view version and will be formally published in a coming issue with other articles in due time.

dual-functional device achieves 23 dB modulation depth in the C-band and responsivity of 0.38 A/W at −2 V. This heterogeneously integrated platform eliminates dependence on monolayer graphene and requires no gate electrodes. Its design flexibility allows it to be used as reconfigurable optical elements in on-chip photonic computing systems. Concurrent optical modulation and real-time electrical readout through dual ports allows in-situ monitoring of modulation states, enabling ultra-compact integrated photonic circuits.

2 Experimental section

2.1 Waveguide fabrication

The bottom layer includes a microring resonator with grating couplers on a silicon-on-insulator (SOI) platform with 220 nm device layer, the height of the ridge waveguide 70 nm, and the slab of 150 nm. Both the straight and ring waveguide have a width of 450 nm and the gap between them is 100 nm. A pair of tapered gratings was designed at both ends of the straight waveguide for efficient coupling for TE mode. All these structures were fabricated by electron beam lithography (EBL) and inductively coupled plasma (ICP) etching processes. Then, the 10 nm thick aluminum oxide (Al_2O_3) dielectric layer between the SOI platform and the SnS_2 is deposited by atomic layer deposition (ALD) which acts as an electrical isolation layer. After this, another step of e-beam lithography is done to define the metal electrodes. The electrodes are made by evaporating 80 nm of Au using an evaporator and lift-off process.

2.2 TMDC fabrication and characterization

Bulk flakes of SnS_2 (Shenzhen Six Carbon Technology Co., Ltd.) are exfoliated via the Scotch tape method onto polydimethylsiloxane (PDMS). Next, the target flakes are found using an optical microscope and transferred to the intended waveguide by dry transfer technique.

Atomic force microscopy (AFM) and optical microscopy were conducted with a Park NX10 AFM and a Nikon LV100ND optical microscope, respectively.

2.3 Device measurements

Device characterization was performed on an edge-coupling platform with polarization-maintaining fibers. Tunable laser light (1520–1620 nm) was coupled into the waveguide via a high-precision alignment stage. Thermo-optic modulation was driven by a programmable DC source (Keysight B2912A) providing bias voltages to Electrodes A/B. Temporal response of the modulation function was captured using a waveform generator and a real-time oscilloscope (Lecroy, 740Zi-A). Photodetection metrics including I-V characteristics and response time were quantified using a semiconductor parameter analyzer (Keysight B1500A) under tunable laser (TUNICS T100S-HP).

3 Results and discussion

3.1 Device fabrication and characterization

Conventional approaches for dual-function devices rely on graphene-based capacitors, FETs, or heterojunctions, where an out-of-plane electric field shifts the band edge to enable functionality. These architectures exhibit critical dependence on graphene thickness and require precise capacitor/heterojunction fabrication[1−3]. In contrast, our design eliminates thickness constraints for SnS_2 and operates without external gate bias, reducing process complexity. Figure 1(a) illustrates the dual functional device of SnS_2 integrated on a microring resonator. We use the two-dimensional (2D) material as an interlayer between the waveguide and the thermally active gold film. This configuration simultaneously reduces the detrimental influence of the gold heater on the optical transmission characteristics of the microring resonator. Achieving infrared photoresponse in wide-bandgap SnS_2 (E_g=2.07 eV) by direct bandgap absorption presents a challenge[26,27]. Here, we overcome this limitation through hot-carrier-assisted detection enabled by micro-ring-enhanced light-matter interactions. At the same time, the wide-bandgap 2D material SnS_2 exhibits minimal absorption within the infrared spectrum, implying negligible perturbation to resonant cavity transmission. Crucially, the incorporation of this photoactive material is essential for photodetection.

All the waveguide structures were fabricated using EBL and ICP etching processes. The SnS_2 was then mechanically exfoliated onto the silicon waveguide. Au electrodes (80 nm-thick) were fabricated through lift-off process. A schematic of the dual-function device architecture is shown in Fig. 1(a). Electrodes A and B were patterned on top of the waveguide and SnS_2 layer for optical modulation, while electrode C was positioned in contact with SnS_2 but far away from the waveguide and modulation electrodes for photodetection. Figure 1(b) shows the microscopy image of the fabricated device. Figure 1(c) shows the Raman spectrum of SnS_2 within the integrated device, which exhibits characteristic vibrational modes at 315 cm^{-1}[28], and the height profile in Fig. 1(d) indicates a thickness of 18.8 nm.

3.2 Thermo-optic modulation operation

To characterize the effect of Al_2O_3, SnS_2 and Au electrode deposition on the ring resonator, the transmission spectrum of the microring resonator was measured at each fabrication step, as shown in Fig. 2(a). During device characterization, we monitored the current between modulation electrodes A and B as a function of DC voltage (Fig. 2(c)). At 6 V applied bias, the modulation electrodes are at risk of thermal

This is an early view version and will be formally published in a coming issue with other articles in due time.

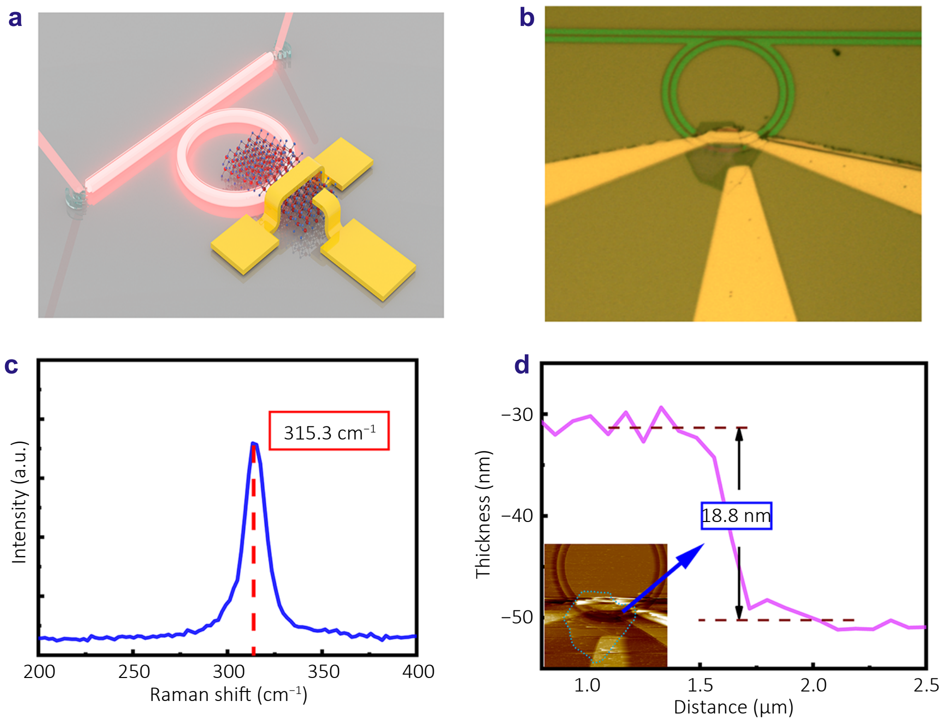

Fig. 1 | (a) Dual-function device architecture for optical modulation and photodetection based on SnS_2 integrating with a microring resonator (MRR). Light is coupled in/out by two opposite grating couplers. (b) Microscope image of the device. (c) Raman spectrum of SnS_2 film. (d) AFM height profile (inset) showing a thickness of 18.8 nm for the SnS_2 flake.

breakdown. To ensure low-power operation and prevent electrode failure, we maintained the loop current below 0.05 A. The transmission spectra under DC voltages of 0.5–1 V applied between electrodes A and B are shown in Fig. 2(b). We observe a redshift of the resonance dip while the extinction ratio remains unchanged. At the resonant wavelength of 1549.76 nm, the device exhibits an extinction ratio of 24 dB and a 3-dB bandwidth of 0.52 nm, corresponding to a quality factor (Q) of 2980. Under the bias of 0.8 V, a modulation depth of 23 dB is achieved. Increasing the bias from 0 to 0.8 V induces a 1.8 nm shift, with a power consumption of 38 mW. The thermo-optic tuning efficiency is calculated as 0.047 nm/mW.

The thermo-optic effect is the physical basis for achieving light modulation in this device: when a bias voltage is applied between electrodes A and B, the temperature of the gold electrode increases and is transferred to SnS_2, thereby increasing the lattice temperature. Consequently, the bottom waveguide is heated and the refractive index changes, inducing a redshift in the transmission spectrum of the microring resonator. The resonant wavelength shift ($\Delta\lambda$) is related to the effective refractive index change (ΔN_{eff}) through Eq. (1). The relationship between temperature and ΔN_{eff} is given by Eq. (2).

$$\Delta\lambda = \frac{\lambda_0 \Delta N_{\mathrm{eff}}}{n_{\mathrm{g}}} \,, \tag{1}$$

$$\Delta N_{\mathrm{eff}} \approx (\mathrm{d}n/\mathrm{d}T)\Delta T \,, \tag{2}$$

where n_{g} and λ_0 are real part of the group index and resonant wavelength, respectively. ΔN_{eff} exhibits a linear dependence on temperature. The corresponding resonant wavelength shift as a function of power is shown in Fig. 2(d). Furthermore, since temperature is linearly proportional to applied power, the resonant wavelength shift is also linearly proportional to the applied power. This conclusion is consistent with the experimental results. Then, we measured the dynamic response of the modulator (shown as in Fig. 2(e)). The square wave modulation signal generated by the function generator had a peak-to-peak voltage of 1 V, applied across the modulation electrodes A and B, with a square wave frequency of 10 kHz. The rise time (from 10% to 90%) was 3.4 μs and the decay time (from 90% to 10%) was 6.9 μs.

3.3 Hot-carrier-assisted photodetection operation

Under non-modulated conditions (U_{ab}=0 V), the current (I_{bc}) between electrode B and electrode C was measured as a function of bias voltage (U_{bc}). By coupling light at a wavelength of 1549.76 nm into the waveguide, photocurrent is observed. The *I*-*V* curves obtained at different optical powers are shown in Fig. 3(a). The asymmetric behavior observed in the *I*-*V* characteristics confirms the formation of back-to-back Schottky barriers. The energy band diagram of the Au/SnS_2/Au interface is shown in Fig. 3(b), where (i)

This is an early view version and will be formally published in a coming issue with other articles in due time.

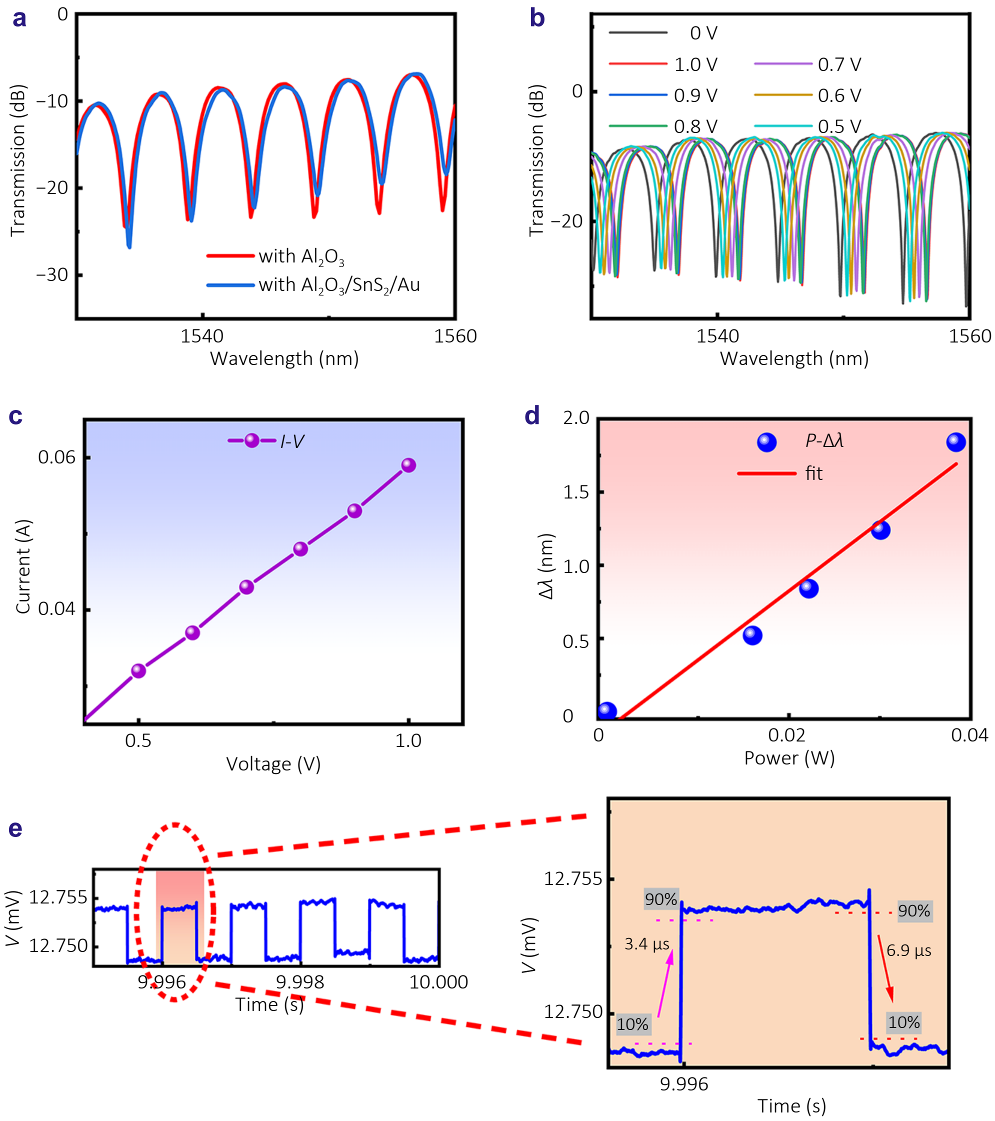

Fig. 2 | (a) Measured transmission spectra of the MRR after each step of transfer. (b) Transmission spectra of an MRR integrating with Au/SnS_2 under different bias voltages. (c) Current variation between electrode A and electrode B as a function of DC voltage. (d) Resonance wavelength shift as a function of electric power. (e) Response time of thermal tuning.

represents the alignment of the Fermi level of Au with that of n-type SnS_2 at equilibrium. (ii, iii) are the energy band diagrams of the device under $U_{bc} < 0$ V and $U_{bc} > 0$ V, respectively. When $U_{bc} < 0$ V, the left metal is grounded and a positive voltage is applied to the right metal. Consequently, the Fermi level of the left metal is higher than that of the right metal. In addition, for the left Au/SnS_2 heterojunction, this is a reverse bias, and for the right Au/SnS_2 heterojunction, it is a forward bias, so the barrier heights of the two junctions are different. When $U_{bc} > 0$ V, the right metal is grounded and a positive voltage is applied to the left metal, the Fermi level of the left metal is lower than the right metal. For the left Au/SnS_2 heterojunction, this is a forward bias; for the right heterojunction, it is a reverse bias. Thus, the two barrier heights are different. When light is coupled to a microring resonant cavity, the Au/SnS_2 interface is in an evanescent field. Because light penetrates multiple times and interacts with SnS_2, energy is ultimately converted into lattice heat through the bolometric (BOL) effect, resulting in a local temperature increase. Hot carriers generated by lattice heating in SnS_2 contribute to the current under bias voltage. In addition, the evanescent field overlapping the electrode B also excites the generation of hot carriers. At zero bias, the built-in electric field of the Au/SnS_2 Schottky junction injects hot carriers into SnS_2, which then diffuse to electrode C. When U_{bc}<0 V, a reverse electric field is established, driving hot carriers to drift from electrode B to electrode C through the SnS_2 channel. On the contrary, when U_{bc}>0 V, the external electric field prevents hot carriers in the metal from injecting into SnS_2 from electrode B.

This is an early view version and will be formally published in a coming issue with other articles in due time.

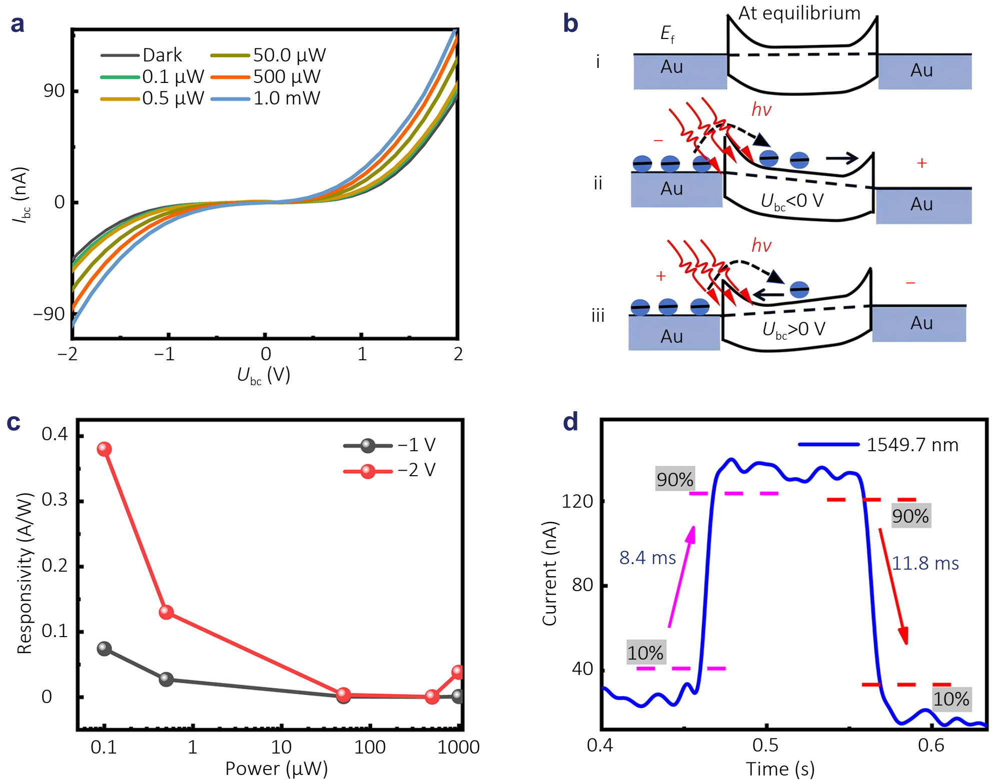

Fig. 3 | (a) I_{bc}-U_{bc} curves at different 1549.76 nm optical powers. (b) Energy band diagram of the photodetection mechanism at equilibrium, under U_{bc}< 0 V and under U_{bc} > 0 V. (c) The responsivity of the Au/SnS_2/Au detector versus incident optical power at −1 V and −2 V. (d) Photocurrent rise and fall times.

Experimental results show that the SnS_2 device exhibits a dark current of 41.7 nA at −2 V bias. As shown in Fig. 3(c), when a 1549.76 nm light source with 0.1 μW optical power is coupled into the waveguide through the grating, the device exhibits a responsivity of 0.38 A/W under −2 V bias. The responsivity increases with the applied bias voltage. In Fig. 3(d), the measured 10%–90% rise time and 90%–10% fall time are 8.4 ms and 11.8 ms, respectively. The measurement was performed using a semiconductor parameter analyzer, with a bias voltage of 2 V applied across electrodes B and C. The input optical power was 1 mW at a wavelength of 1549.76 nm, and the laser was switched on and off to obtain the temporal response.

3.4 Mechanism of synergistic current dynamics in dual-mode operation

Additionally, with a DC bias applied between electrodes A and B for modulation, the output current between electrode B and electrode C was measured while 1549.76 nm laser was coupled into the waveguide. Figure 4(a) shows the equivalent circuit for synchronous optical modulation and detection. The corresponding results are shown in Fig. 4(b). These results indicate that applying different voltages between electrodes A and B affects the output current between electrodes B and C. Figure 4(c) shows that increasing U_{ab} enhances output current I when U_{bc} < 0 V. Conversely, increasing U_{ab} reduces output current I when U_{bc} > 0 V (Fig. 4(d)).

This phenomenon originates from the synergistic coupling between thermal and electric fields in the Au/SnS_2/Au (MSM structure). With the modulation voltage U_{ab} increasing, the resonant wavelength undergoes a red shift, resulting in reduced light intensity in the microring resonant cavity, and a corresponding decrease in I_{bc}. When U_{ab} is applied across electrodes A and B, the temperature at electrode B increases, leading to two key physical effects. First, due to the Seebeck effect, the temperature gradient ∇T between electrode B and electrode C generates a thermoelectric potential in SnS_2, driving electrons to diffuse from the high-temperature region (electrode B) to the low-temperature region (electrode C), forming a thermally induced diffusion current I_{diff} directed from C to B. Second, in the MSM structure, the two Au/SnS_2 Schottky junctions are connected back-to-back in series. When U_{bc} < 0 V, the reverse-biased junction is located at electrode B, while the Schottky junction at electrode C is forward-biased. The local temperature rise increases the concentration of thermally excited carriers near electrode B. Consequently, the thermally excited carriers near electrode B contribute an additional current component $I_{enhanced}$ under the applied electric field. In this case, I_{diff} is in the same direction as the drift

This is an early view version and will be formally published in a coming issue with other articles in due time.

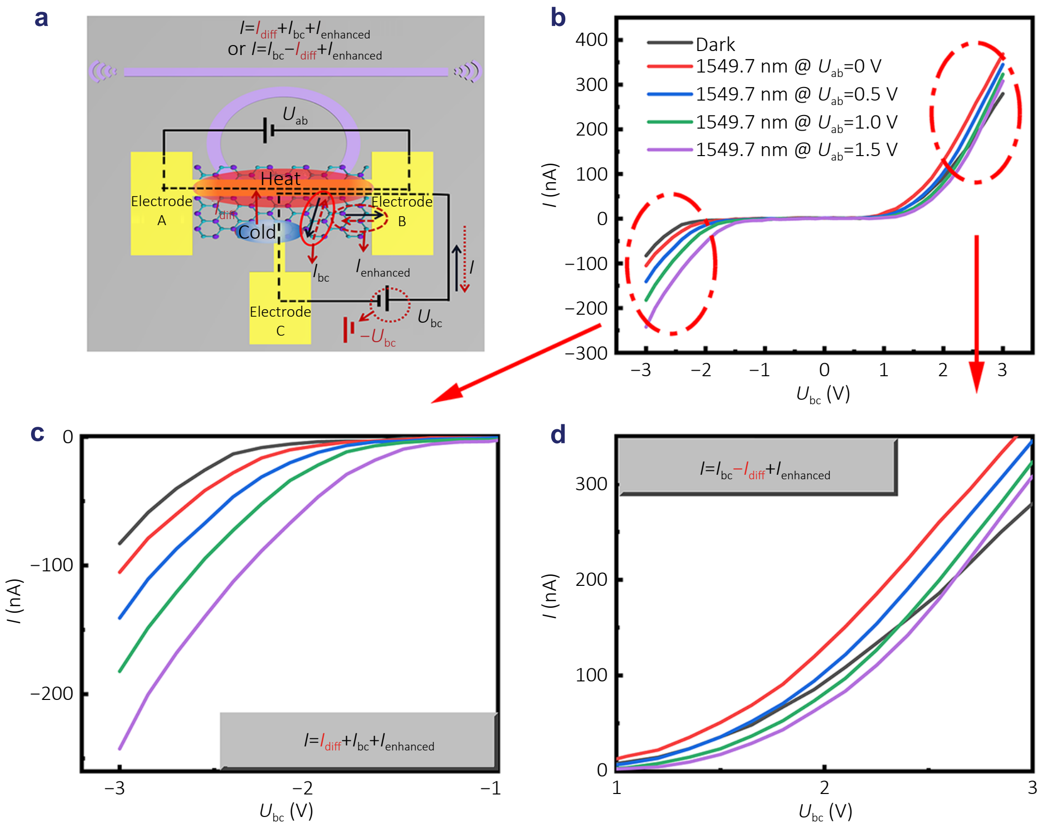

Fig. 4 | (a) Equivalent circuit diagram for synchronous optical modulation and detection. (b) I-U_{bc} characteristics at different modulation voltages U_{ab}. (c) I-U_{bc} characteristics at U_{bc} < 0 V. (d) I-U_{bc} characteristics at U_{bc} > 0 V.

current I_{bc} (both from C to B). Therefore, the total current $I = I_{bc} + I_{diff} + I_{enhanced}$. Among the three components, only I_{bc} decreases with the increase of U_{ab}. As the experimental results show that the total current I increases with U_{ab}, it can be inferred that the decrease in I_{bc} is smaller than the increase in I_{diff} and $I_{enhanced}$, as shown in Fig. 5(a). When U_{bc} > 0 V, the reverse-biased junction is located at electrode C, while the Schottky junction at electrode B is forward-biased. The thermally excited carriers near electrode B also contribute an additional current component $I_{enhanced}$ under the applied electric field. However, in this case, I_{diff} is opposite in direction to I_{bc}. Therefore, the total current $I = I_{bc} - I_{diff} + I_{enhanced}$. Experimental results show that I decreases with increasing U_{ab}, indicating that the increase in I_{diff} is larger than that in $I_{enhanced}$, as illustrated in Fig. 5(b).

3.5 Performance optimization and integration prospects

This dual-functional device integrates optical modulation and real-time photocurrent readout through its dual-port electrode design. Crucially, the output current at the detection port (Electrodes B/C) provides in situ monitoring of the modulation state. By establishing the correlation between modulation voltage (Electrodes A/B) and output current I, we demonstrate a voltage-to-current feedback mechanism. Figure 6 shows a schematic diagram of this real-time feedback monitoring using the dual-functional unit device.

When this device is applied in on-chip optical computing systems, its dual-port electrode design enables real-time crosstalk monitoring between devices, thereby improving computational accuracy through dynamic feedback control. However, further research and optimization are still required in terms of thermo-optic modulation efficiency, dark current suppression, and speed. Regarding thermo-optic tuning efficiency, the current device achieves a value of 0.047 nm/mW. While this is sufficient for a proof-of-concept demonstration, the efficiency can be improved by employing suspended structures[29], air trench isolation[30,31], and high-resistivity heater materials such as TiN or IHO[32,33]. For dark current suppression, the measured dark current of 41.7 nA at −2 V bias originates primarily from hot-carrier injection and trap-assisted tunneling. Suppression strategies include inserting a thin high-κ dielectric layer (Al_2O_3 or HfO_2) between the metal and SnS_2, reducing the electrode contact area, or constructing van der Waals heterostructures[34–37]. Besides, the photodetection response time is on the millisecond scale, and the modulator response time is on the microsecond scale. The current speeds are suitable for applications such as optical power monitoring, neuromorphic

This is an early view version and will be formally published in a coming issue with other articles in due time.

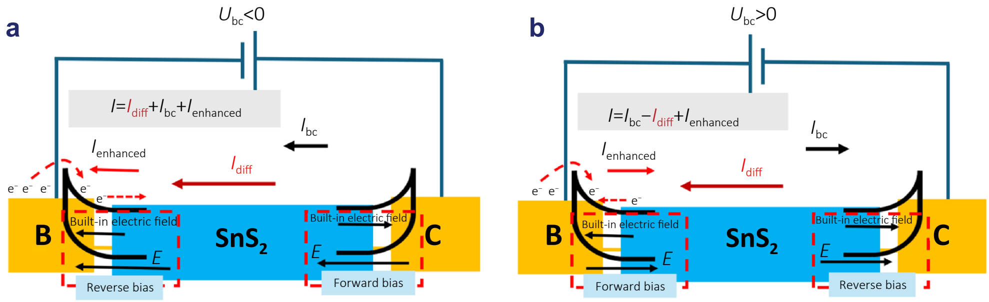

Fig. 5 | (a) Equivalent circuit diagram for U_{bc} < 0 V. (b) Equivalent circuit diagram for U_{bc} > 0 V.

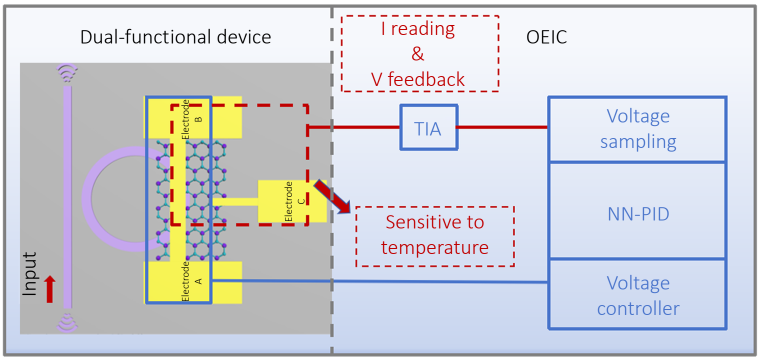

Fig. 6 | Schematic diagram of real-time feedback monitoring.

computing, and artificial synapses[38,39]. If the device is to be used in on-chip high-speed optical computing systems, the electrode geometry should be optimized to reduce carrier diffusion time, and the SnS_2 thickness should be decreased to lower the RC time constant. Alternatively, plasmonic resonance effects could be introduced to enable operation in the GHz frequency range[40].

In addition to the device-level comparison presented in Table 1, material selection is a key factor influencing overall device performance and scalability. Table 2 compares our device with five representative platforms (graphene, $MoTe_2$, black phosphorus, plasma-doped Si, Ge-on-Si) on optical loss, integration complexity, advantages, and limitations. The comparison shows that conventional approaches, while capable of high speed or high responsivity, are accompanied by high optical loss, complex epitaxial growth, and thermal management issues. In contrast, our device combines low optical loss with simplified integration. More importantly, the heterogeneous integration of SnS_2 with a silicon microring resonator enables both detection and modulation in a single device, improving the integration density and stability of on-chip optical computing systems. Although the current device uses mechanically exfoliated SnS_2, with the continued maturation of two-dimensional material growth and transfer technologies[46,47], the proposed scheme is expected to achieve large-scale, high-density integration.

4 Conclusions

In summary, we demonstrate a compact SnS_2-based dual-functional device integrated with a microring resonator that simultaneously achieves optical modulation and photodetection through electrode design, eliminating the need for conventional gate-voltage control or heterojunction

Table 2 | Material platform comparison.

Material	Optical loss (C-band)	Integration complexity	Key advantage	Key limitation	Ref.
Graphene	High	Medium	High speed	Monolayer dependence	ref.[3,5]
$MoTe_2$	Moderate	Medium	Moderate speed	Strain-engineered detection; heterojunction required for modulation	ref.[4,41]
BP	High	Medium	High responsivity	Oxidation-prone	ref.[42,43]
Plasma-doped Si	Low	High (CMOS)	High speed	High thermal budget	ref.[25,44]
Ge-on-Si	Low	High (epitaxy)	High responsivity	Lattice mismatch	ref.[45]
SnS_2	Low	Medium	Simultaneous dual-function; High responsivity	Millisecond-scale response time	This work

This is an early view version and will be formally published in a coming issue with other articles in due time.

structures and thereby simplifying fabrication and enhancing system integration density. The device achieves a modulation depth of 23 dB and a responsivity of 0.38 A/W for infrared photodetection at −2 V bias. This design paradigm, applicable to diverse 2D materials, extends their applicability in silicon photonics and, with further optimization, could address the requirements of next-generation computing. Furthermore, it enables real-time monitoring of the modulation state through photocurrent readout (using electrodes B and C) and enhances system stability by feedback-driven crosstalk suppression, thereby establishing a scalable pathway toward reliable multifunctional photonic integrated circuits.

References

1. Asakawa K, Sugimoto Y, Nakamura S. Silicon photonics for telecom and data-com applications. *Opto-Electron Adv* **3**, 200011 (2020).
2. Wang YD, Wang YW, Dong YL et al. 2D Nb_2CT_x MXene/MoS_2 heterostructure construction for nonlinear optical absorption modulation. *Opto-Electron Adv* **6**, 220162 (2023).
3. Zhong CY, Liao K, Dai TX et al. Graphene/silicon heterojunction for reconfigurable phase-relevant activation function in coherent optical neural networks. *Nat Commun* **14**, 6939 (2023).
4. Wu JH, Jian JL, Sun BS et al. Dual-function optical modulation and detection in microring resonators integrated graphene/$MoTe_2$ heterojunction. *Appl Phys Rev* **11**, 021426 (2024).
5. Youngblood N, Anugrah Y, Ma R et al. Multifunctional graphene optical modulator and photodetector integrated on silicon waveguides. *Nano Lett* **14**, 2741–2746 (2014).
6. Sun S, Zhang RY, Peng JX et al. MO detector (MOD): a dual-function optical modulator-detector for on-chip communication. *Opt Express* **26**, 8252–8259 (2018).
7. Huang GY, Hao YB, Li SQ et al. Recent progress in waveguide-integrated photodetectors based on 2D materials for infrared detection. *J Phys D: Appl Phys* **56**, 113001 (2023).
8. Cheng Z, Cao R, Guo J et al. Phosphorene-assisted silicon photonic modulator with fast response time. *Nanophotonics* **9**, 1973–1979 (2020).
9. Wang YZ, Zhang F, Tang X et al. All-optical phosphorene phase modulator with enhanced stability under ambient conditions. *Laser Photonics Rev* **12**, 1800016 (2018).
10. Lin C, Grassi R, Low T et al. Multilayer black phosphorus as a versatile mid-infrared electro-optic material. *Nano Lett* **16**, 1683–1689 (2016).
11. Li ZW, Hu SQ, Zhang Q et al. Telecom-band waveguide-integrated MoS_2 photodetector assisted by hot electrons. *ACS Photonics* **9**, 282–289 (2022).
12. Li CH, Du W, Huang YX et al. Photonic synapses with ultralow energy consumption for artificial visual perception and brain storage. *Opto-Electron Adv* **5**, 210069 (2022).
13. Wei KK, Li DL, Lin ZT et al. All-optical $PtSe_2$ silicon photonic modulator with ultra-high stability. *Photonics Res* **8**, 1189–1196 (2020).
14. Gherabli R, Indukuri SRKC, Zektzer R et al. $MoSe_2$/WS_2 heterojunction photodiode integrated with a silicon nitride waveguide for near infrared light detection with high responsivity. *Light Sci Appl* **12**, 60 (2023).
15. Guan XW, Yu XC, Periyanagounder D et al. Recent progress in short-to long-wave infrared photodetection using 2D materials and heterostructures. *Adv Opt Mater* **9**, 2001708 (2021).
16. He X, Wang YL, Peng ZR et al. On-chip two-dimensional material-based waveguide-integrated photodetectors. *J Mater Chem C* **12**, 2279–2316 (2024).
17. Chen HT, Wang C, Ouyang H et al. All-optical modulation with 2D layered materials: status and prospects. *Nanophotonics* **9**, 2107–2124 (2020).
18. Liu CY, Guo JS, Yu LW et al. Silicon/2D-material photodetectors: from near-infrared to mid-infrared. *Light Sci Appl* **10**, 123 (2021).
19. Gan XT, Englund D, Van Thourhout D et al. 2D materials-enabled optical modulators: from visible to terahertz spectral range. *Appl Phys Rev* **9**, 021302 (2022).
20. Wu JY, Yang YY, Qu Y et al. Graphene oxide waveguide and micro-ring resonator polarizers. *Laser Photonics Rev* **13**, 1900056 (2019).
21. Yan SQ, Zuo Y, Xiao SS et al. Graphene photodetector employing double slot structure with enhanced responsivity and large bandwidth. *Opto-Electron Adv* **5**, 210159 (2022).
22. Elshahat DR, Areed NF, Yousif B et al. Broadband low-loss efficient optical plasmonic modulator based on graphene and bowtie-shape waveguide. *Opt Quant Electron* **55**, 481 (2023).
23. Gan S, Cheng CT, Zhan YH et al. A highly efficient thermo-optic microring modulator assisted by graphene. *Nanoscale* **7**, 20249–20255 (2015).
24. Edelstein S, Indukuri SRKC, Mazurski N et al. Waveguide-integrated mid-IR photodetector and all-optical modulator based on interlayer excitons absorption in a WS_2/HfS_2 heterostructure. *Nanophotonics* **11**, 4337–4345 (2022).
25. Yang X, Ran SH, Li ZQ et al. Field programmable silicon microring WDM transceiver leveraging monolithically integrated phase-change materials. *PhotoniX* **6**, 16 (2025).
26. Domingo G, Itoga RS, Kannewurf CR. Fundamental optical absorption in SnS_2 and $SnSe_2$. *Phys Rev* **143**, 536–541 (1966).
27. Liu Z, Jia XY, Duan WS et al. High photoresponsivity and response speed of visible-light photodetectors based on tin disulfide/indium-doped tin disulfide homostructures. *Adv Opt Mater* **11**, 2202087 (2023).
28. Hu Y, Chen T, Wang XQ et al. Controlled growth and photoconductive properties of hexagonal SnS_2 nanoflakes with mesa-shaped atomic steps. *Nano Res* **10**, 1434–1447 (2017).
29. Dong PH, Zhang L, Dai DX et al. All-optical switching of silicon nanobeam cavities with an ultra-compact heater utilizing the photothermal effect. *ACS Photonics* **9**, 197–202 (2022).
30. Ning NN, Zhang Q, Huang QK et al. Thermal flux manipulation on the silicon photonic chip to suppress the thermal crosstalk. *APL Photonics* **9**, 046108 (2024).
31. De S, Das R, Varshney RK et al. CMOS-compatible photonic phase shifters with extremely low thermal crosstalk performance. *J Lightwave Technol* **39**, 2113–2122 (2021).
32. Krause EE, Malka D. Optimizations of double titanium nitride thermo-optic phase-shifter heaters using SOI technology. *Sensors* **23**, 8587 (2023).
33. Tong WY, Yang EQ, Dong J et al. An efficient, fast-responding, low-loss thermo-optic phase shifter based on a hydrogen-doped indium oxide microheater. *Laser Photonics Rev* **17**, 2201032 (2023).
34. Wriedt N, Meng LY, Yu DS et al. Enhanced UV-Vis rejection ratio in metal/$BaTiO_3$/β-Ga_2O_3 solar-blind photodetectors. *Adv Electron Mater* **11**, 2400552 (2025).
35. Rezeq M, Eledlebi K, Ismail M et al. Theoretical and experimental investigations of nano-Schottky contacts. *J Appl Phys* **120**, 044302 (2016).
36. Huang Y, Deng HX, Xu K et al. Highly sensitive and fast phototransistor based on large size CVD-grown SnS_2 nanosheets. *Nanoscale* **7**, 14093–14099 (2015).
37. Liu X, Deng CY, Wei H et al. High-sensitive uncooled mid-wave infrared photodetector based on $PtSe_2$/$MoTe_2$ heterojunction with fast speed. *Adv Funct Mater* **35**, 2423102 (2025).
38. Ochiai T, Akazawa T, Miyatake Y et al. Ultrahigh-responsivity

This is an early view version and will be formally published in a coming issue with other articles in due time.

waveguide-coupled optical power monitor for Si photonic circuits operating at near-infrared wavelengths. *Nat Commun* **13**, 7443 (2022).
39. Jiang M, Zhao YK, Liu T et al. A dual-mode transparent device for 360° quasi-omnidirectional self-driven photodetection and efficient ultralow-power neuromorphic computing. *Light Sci Appl* **14**, 273 (2025).
40. Guo JS, Li J, Liu CY et al. High-performance silicon-graphene hybrid plasmonic waveguide photodetectors beyond 1.55 μm. *Light Sci Appl* **9**, 29 (2020).
41. Maiti R, Patil C, Saadi MASR et al. Strain-engineered high-responsivity $MoTe_2$ photodetector for silicon photonic integrated circuits. *Nat Photonics* **14**, 578–584 (2020).
42. Ma YM, Dong BW, Wei JX et al. High-responsivity mid-infrared black phosphorus slow light waveguide photodetector. *Adv Opt Mater* **8**, 2000337 (2020).
43. Huang WC, Yang YM, Zhang H. Surface engineering of two-dimensional black phosphorus for advanced nanophotonics. *Acc Chem Res* **57**, 2464–2475 (2024).
44. De S, Das R, Varshney RK et al. Design and simulation of thermo-optic phase shifters with low thermal crosstalk for dense photonic integration. *IEEE Access* **8**, 141632–141640 (2020).
45. Zhao DY, Shao YL, Zhang S et al. Impact of charge carrier trapping at the Ge/Si interface on charge transport in Ge-on-Si photodetectors. *Electronics* **14**, 2982 (2025).
46. Liu LW, Cai ZG, Xue SW et al. A mass transfer technology for high-density two-dimensional device integration. *Nat Electron* **8**, 135–146 (2025).
47. Zheng XD, Wang JT, Jiang JF et al. Electrostatic-repulsion-based transfer of van der Waals materials. *Nature* **645**, 906–914 (2025).

Acknowledgements

This research was funded by the National Natural Science Foundation of China (62205029); the National Key Research and Development Sub project (2022YFF0705801); the Young Elite Scientists Sponsorship Program by CAST (2022QNRC001).

Author contributions

All authors commented on the manuscript. Jinyi Du proposed the initial idea and supervised the project. Lianqing Zhu, Lidan Lu, Bofei Zhu, Xu Zhang, Guanghui Ren and Zheng You supervised the project, while other authors guided the work, with equal contributions.

Competing interests

The authors declare no competing financial interests.

Open Access This article is licensed under a Creative Commons Attribution 4.0 International License, which permits use, sharing, adaptation, distribution and reproduction in any medium or format, as long as you give appropriate credit to the original author(s) and the source, provide a link to the Creative Commons license, and indicate if changes were made. To view a copy of this license, visit http://creativecommons.org/licenses/by/4.0/
©The Author(s) 2026.
Published by Editorial Office of *Opto-Electronic Advance*, Institute of Optics and Electronics, Chinese Academy of Sciences.

Opto-Electronic Journals Group
www.oejournal.org
Scan for Article PDF

This is an early view version and will be formally published in a coming issue with other articles in due time.